doi.org/10.15392/2319-0612.2026.3075
Braz. J. Radiat. Sci., Rio de Janeiro
Jul-Sep 2026, 14(3) | 01-21 | e3075
Editor(s): Dr. (Prof.) Bernardo Maranhão Dantas
Dr. (Prof.) Alfredo L. Ferreira Filho
Prof Dr Fernando Roberto de Andrade Lima
Submitted: 2026-02-27
Accepted: 2026-09-21

Modeling and Implementation of an Automated Gamma Radiography Inspection System with Robotic Positioning and Bidimensional Radiative Mapping in Cartesian Coordinates

Silva[a*], L. M. C.; Silveira[a], P. C. R.

[a] Instituto Militar de Engenharia (IME), 22290-270, Rio de Janeiro, RJ, Brazil.

*Correspondence: leandro.moreira@ime.eb.br

Abstract: This work presents the engineering architecture and controlled radiometric evaluation of a gamma-ray inspection system conceived for Cartesian X-Y automation in non-destructive testing of metallic plates. The architecture combines a Cadmium Zinc Telluride (CZT) detector, a collimated Cesium-137 source, lead shielding, Cartesian positioning, and computational mapping. The radiometric dataset reported here was acquired before complete motion integration: the source and detector remained fixed while aluminum plates of nominal 200 x 200 mm and 1 mm or 2 mm thickness were manually repositioned over a 4 x 4 grid. Three consecutive count-rate readings were averaged at each of the sixteen points and corrected using the recorded point-specific background. The resulting net count rates were associated with Cartesian coordinates and displayed as non-interpolated two-dimensional maps. Net count rates ranged from 1206.00 to 2213.67 cps for the 1 mm specimen and from 1538.00 to 2264.67 cps for the 2 mm specimen. Within each specimen, grouped values increased with the inferred open-hole condition; however, the two thickness series were non-monotonic and cannot be interpreted as an isolated thickness effect. For 662 keV photons in aluminum, the ideal narrow-beam Beer-Lambert model predicts transmissions of approximately 98.0% and 96.1% for 1 mm and 2 mm, respectively. Because a no-sample reference and complete pointwise uncertainty data were not available, absolute thickness, detection limit, and statistical significance were not claimed. The study therefore validates the acquisition-background-coordinate-mapping workflow and defines the metrological requirements for subsequent validation of the fully automated platform.

Keywords: Industrial radiography; gamma-ray transmission; CZT detector; radiometric mapping; Cartesian positioning; Cesium-137; non-destructive testing.

doi.org/10.15392/2319-0612.2026.3075
Braz. J. Radiat. Sci., Rio de Janeiro
Jul-Sep 2026, 14(3) | 01-21 | e3075
Editor(s): Dr. (Prof.) Bernardo Maranhão Dantas
Dr. (Prof.) Alfredo L. Ferreira Filho
Prof Dr Fernando Roberto de Andrade Lima
Submitted: 2026-02-27
Accepted: 2026-09-21

Modelagem e Implementação de um Sistema Automatizado de Inspeção por Gamagrafia com Posicionamento Robótico Cartesiano e Mapeamento Radiativo Bidimensional

Resumo: Este trabalho apresenta a arquitetura de engenharia e a avaliação radiométrica controlada de um sistema de inspeção por radiação gama concebido para automação cartesiana X-Y em ensaios não destrutivos de chapas metálicas. A arquitetura combina detector semicondutor de Telureto de Cádmio-Zinco (CZT), fonte colimada de Césio-137, blindagem de chumbo, posicionamento cartesiano e processamento computacional. O conjunto de dados radiométricos apresentado foi obtido antes da integração completa do movimento: fonte e detector permaneceram fixos, enquanto chapas de alumínio com dimensões nominais de 200 x 200 mm e espessuras de 1 mm e 2 mm foram reposicionadas manualmente sobre uma malha 4 x 4. Em cada um dos dezesseis pontos, três leituras consecutivas de taxa de contagem foram promediadas e corrigidas pelo background específico registrado para o ponto. As taxas líquidas foram associadas às coordenadas cartesianas e apresentadas em mapas bidimensionais sem interpolação além das dezesseis células medidas. As taxas líquidas variaram de 1206,00 a 2213,67 cps para a chapa de 1 mm e de 1538,00 a 2264,67 cps para a chapa de 2 mm. Dentro de cada amostra, as médias agrupadas aumentaram com a condição inferida de maior abertura; entretanto, as duas séries de espessura apresentaram resposta não monotônica e não podem ser interpretadas como efeito isolado da espessura. Para fótons de 662 keV no alumínio, o modelo ideal de Beer-Lambert em feixe estreito prevê transmissões de aproximadamente 98,0% e 96,1% para 1 mm e 2 mm, respectivamente. Como não foram preservadas uma referência sem amostra e todas as informações necessárias à incerteza ponto a ponto, não são reivindicadas estimativa absoluta de espessura, limite de detecção ou significância estatística. Assim, o estudo valida o fluxo de aquisição-correção de background-associação coordenada-mapeamento e estabelece os requisitos metrológicos para a validação posterior da plataforma totalmente automatizada.

Palavras-chave: Radiografia industrial; transmissão de radiação gama; detector CZT; mapeamento radiométrico; posicionamento cartesiano; Césio-137; ensaios não destrutivos.

1. INTRODUCTION

Non-destructive testing (NDT) is widely used to assess industrial components without impairing their future service, and radiographic methods remain important when internal information is required [1,2]. In gamma-ray transmission measurements, the signal recorded downstream of a specimen depends on photon attenuation, material composition, density, effective thickness, measurement geometry, and scattering [3,9]. Consequently, spatial interpretation requires controlled geometry and traceable association between each detector response and the physical region that produced it.

Automation can support programmed scanning trajectories and structured spatial registration, but the potential benefits of robotic positioning must be distinguished from experimentally demonstrated performance. Robotic radiation-mapping studies have shown the value of associating detector measurements with spatial coordinates [4], while recent work in robotic radiography has emphasized that motion and geometry can directly affect the acquired radiographic information [6]. Therefore, positioning accuracy, sampling spacing, and effective radiographic spatial resolution are separate quantities and should be validated independently.

Cadmium Zinc Telluride (CZT) detectors are attractive for compact gamma-ray instrumentation because they operate at room temperature and may provide count-rate or spectrometric information [5,7]. Studies using transmitted gamma photons and Cs-137 sources demonstrate their potential for non-destructive testing [5]. In the present experiment, however, the detector was used as a radiometric count-rate monitor; no quantitative energy calibration, dose calibration, or spectrometric window analysis was available for the reported dataset.

The scientific gap addressed here is therefore not a claim that automated inspection is intrinsically superior to conventional gamma radiography. Rather, the work evaluates the measurement chain required before such a comparison can be made: predefined spatial positions, repeatable data registration, background correction, coordinate association, and two-dimensional representation of the measured response. The broader engineering project includes an X-Y Cartesian motion architecture [11], but the radiometric data analyzed in this manuscript were collected before complete integration of the motion system.

Accordingly, the objective of this study is to evaluate whether a controlled 4 x 4 acquisition procedure using a collimated Cs-137 source and a CZT detector can produce traceable two-dimensional radiometric maps for nominal 1 mm and 2 mm aluminum specimens containing artificial perforations. A secondary objective is to compare the experimental response with the theoretical Beer-Lambert attenuation trend and to identify the additional measurements required for quantitative thickness estimation, defect-detection limits, and future validation of the fully automated platform. Quantitative superiority over manual radiography and occupational dose reduction are outside the scope of the present dataset.

2. MATERIALS AND METHODS

2.1. Study design and methodological scope

The study was organized at two levels. The first is an engineering architecture for automated inspection, comprising a Cartesian X-Y positioning stage, stepper-motor control, a collimated gamma source, a CZT detector, and computational processing. The stage design provides a nominal 1 mm command increment; this mechanical command increment is not treated as the effective radiographic spatial resolution. The second level is the controlled radiometric experiment reported here. During that experiment, the source and detector remained fixed and each plate was manually repositioned over sixteen predefined locations. The reported data therefore validate the acquisition and mapping logic, not the positioning accuracy, mechanical repeatability, cycle time, or dose reduction of the automated stage.

2.2. Gamma-ray source, shielding, and collimation

A sealed Cs-137 source was employed, with a principal photon energy of approximately 662 keV. The source label available in the experimental record indicated an initial activity of 5.05 μCi on 15 April 1998. The activity was used only to characterize the source; count rates were not converted to dose. The source was installed in a nominally cubic lead shielding/collimation assembly measuring approximately 120 × 120 × 120 mm, with a nominal central channel diameter of 20.0 mm. The effective lead thickness around the channel and the detailed internal source position were not characterized as a qualified shielding model, and these construction dimensions are therefore reported only as experimental configuration data.

2.3. CZT detector and acquisition system

A Cadmium Zinc Telluride semiconductor detector was connected to its acquisition computer and operated in count-rate mode. The acquisition software displayed a renewed value in counts per second (cps) every 3 s. Three consecutive displayed readings were recorded at each grid point, corresponding to a minimum observation period of approximately 9 s, excluding repositioning and stabilization. The recovered experimental documentation did not preserve the detector model, manufacturer, crystal dimensions, calibrated energy resolution, internal integration time, or energy window used. No independent energy calibration at the 661.7 keV Cs-137 photopeak, dose calibration, or quantitative scatter separation was performed. These missing characteristics are explicitly treated as methodological limitations rather than inferred values.

2.4. Aluminum specimens and Cartesian grid

Two polished aluminum plates with nominal plan dimensions of 200 x 200 mm and nominal thicknesses of 1 mm and 2 mm were examined. The specimens included artificial perforations with nominal diameters of 0.5 mm, 1.0 mm, and 2.0 mm. The original metrological record linking every Cartesian coordinate to a certified individual hole diameter was not preserved. Photographic documentation, specimen marking orientation, and the progression of grouped responses support an inferred correspondence between rows of the grid and reference/nominal-hole conditions. This correspondence is shown explicitly in Figure 3 and is treated as inferential rather than as a certified dimensional identification of each discontinuity.

Figure 1. Annotated experimental arrangement used for the controlled radiometric validation. The source and CZT detector remained fixed while the specimen was manually repositioned. Labels identify the main elements of the acquisition, alignment, detection, and mechanical support assembly. (Authors' own image).

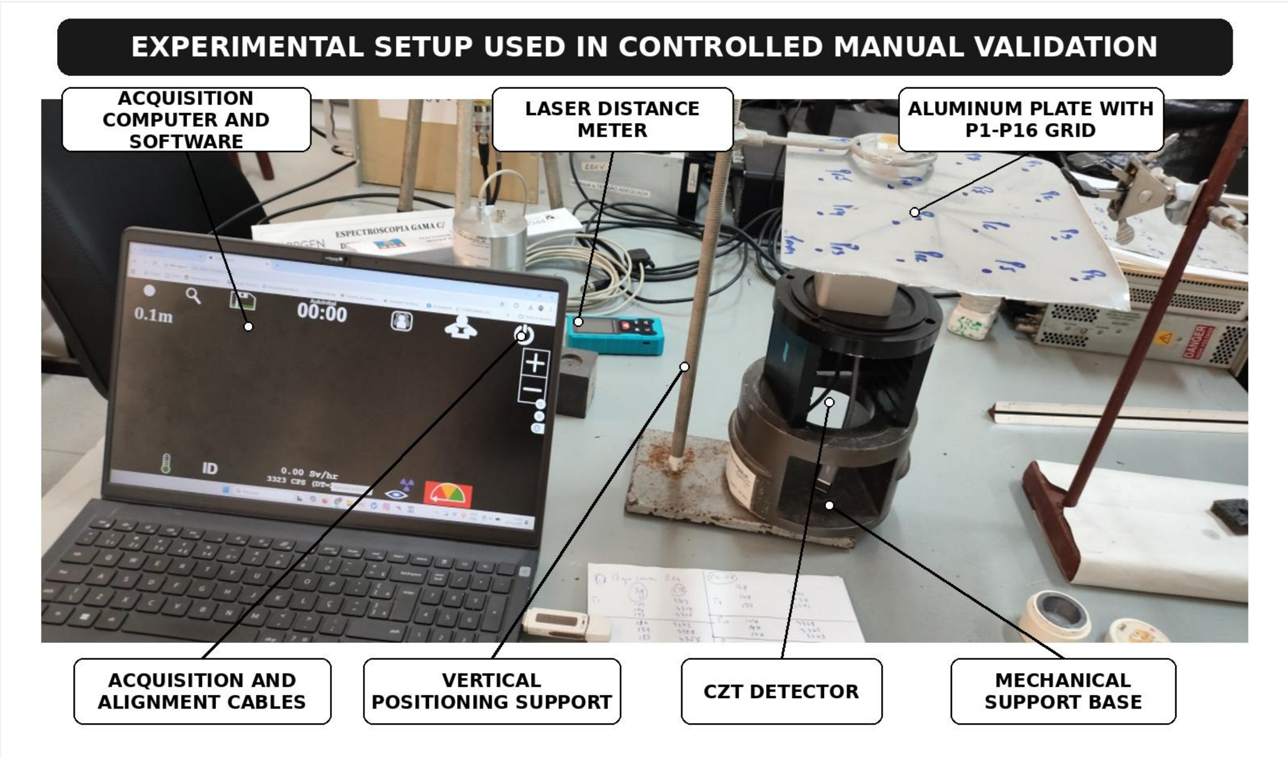

Figure 2. Actual aluminum specimens used in the experiment, aligned for visual comparison: (a) nominal 1 mm plate and (b) nominal 2 mm plate. The marked P1-P16 positions correspond to the 4 x 4 acquisition grid. The point-to-hole correspondence used in the analysis remains inferential based on the recovered experimental record. (Authors' own image).

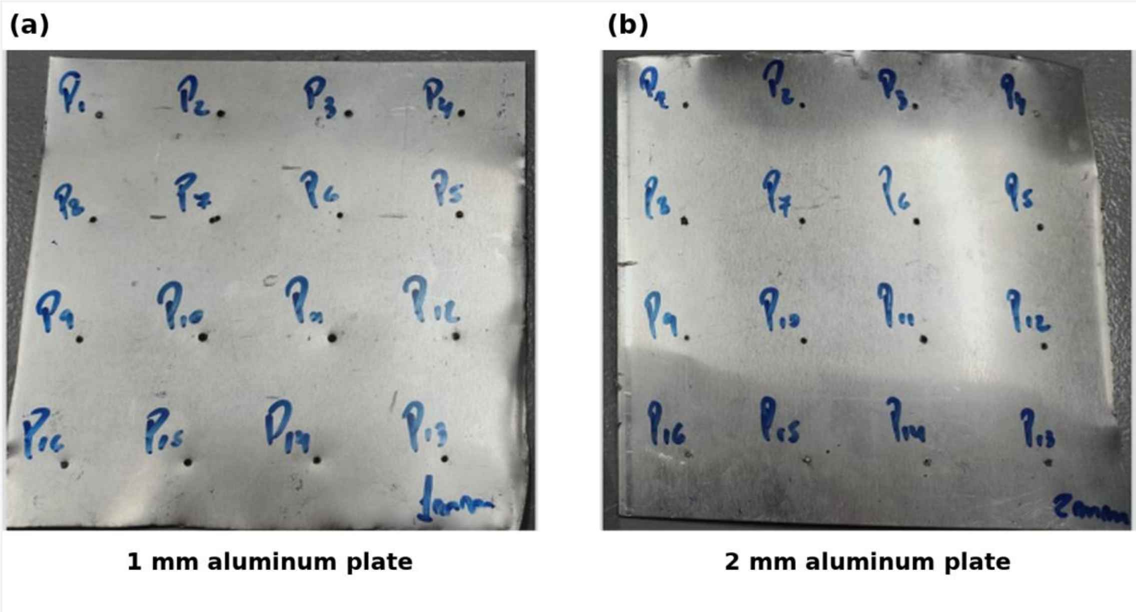

Figure 3. Nominal 4 x 4 Cartesian grid, serpentine acquisition sequence, and inferred row-to-condition correspondence for the two specimens. The hole-condition correspondence is not a dimensionally certified point-by-point defect map.

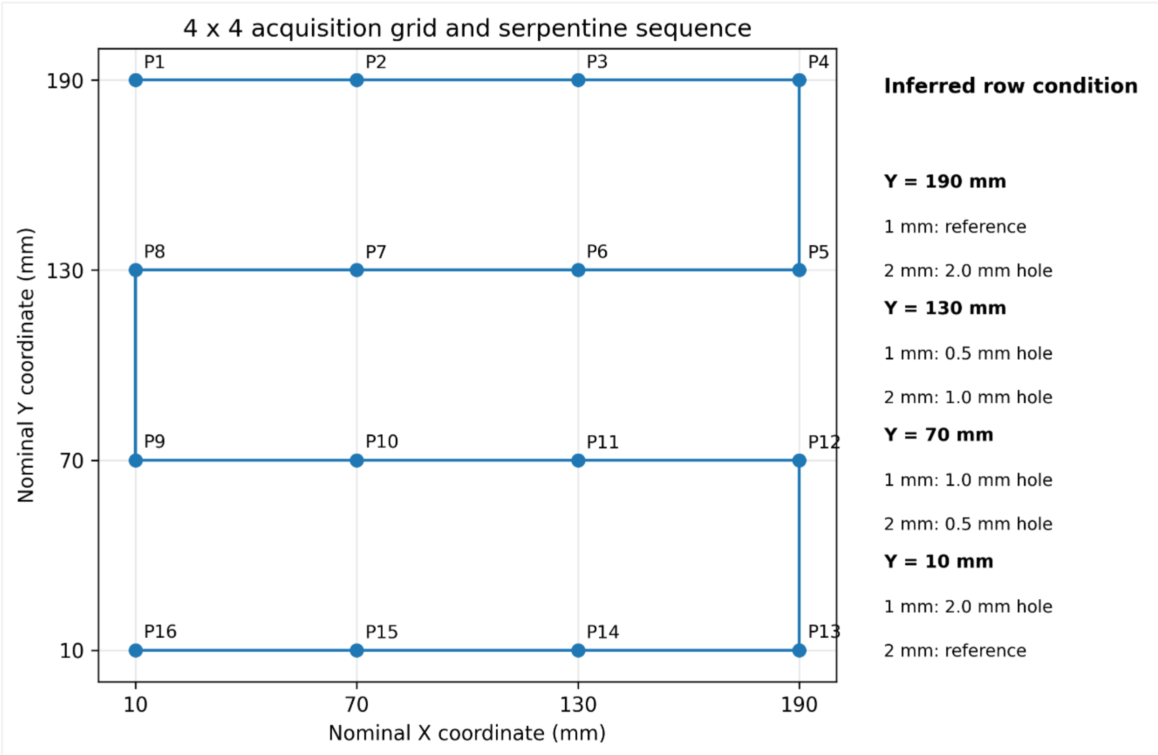

The sixteen positions P1-P16 were arranged on the nominal coordinates shown in Figure 3. Adjacent nominal grid positions were separated by 60 mm in X or Y, while the broader motion-system design had a 1 mm command increment. Sampling spacing, mechanical positioning capability, and effective radiographic spatial resolution are therefore reported as distinct concepts. The effective radiographic resolution was not measured in the present experiment and also depends on collimation, detector sensitive area, source-object-detector geometry, scattering, and data processing.

2.5. Alignment and controlled measurement procedure

The collimated source and the CZT detector were kept fixed throughout the radiometric acquisition. A laser distance meter provided a visual alignment reference to the central marking on the detector. A nominal assembly gap of approximately 1.0 cm was documented between the lower face of the source-support base and the upper surface of the detector; this observation was a photographic assembly check rather than a calibrated source-to-detector distance. Each plate was manually repositioned so that the selected region intersected the fixed beam. Consequently, the general arrangement was maintained, but the uncertainty associated with manual specimen repositioning was not independently quantified.

At 662 keV, attenuation in aluminum includes interactions that remove photons from the primary beam, while photons scattered in the specimen or surrounding structures may still reach a finite detector aperture. The experiment did not separately measure the scattered component. Thus, the recorded CZT count rate is treated as the response of the complete experimental geometry rather than as a pure narrow-beam primary transmission measurement [3,9].

2.6. Data processing, background correction, and statistical treatment

For each grid point j, the source-present count-rate value used in the analysis was the arithmetic mean of three consecutive displayed readings. The previous description of a weighted average was removed because no unequal statistical weights were defined in the recovered record. The net response was obtained by subtracting the recorded point-specific background from the source-present mean:

$$C_{F,j} = (1/3)\ \Sigma_{i=1}^{3}\ C_{F,ij} \qquad (1)$$

$$C_{net,j} = C_{F,j} - C_{BG,j} \qquad (2)$$

where C(F,j) is the arithmetic mean of the three source-present readings, C(BG,j) is the recorded background associated with that point, and C(net,j) is the net count rate. Reprocessing of the consolidated experimental record corrected a preliminary treatment in which an uncertainty-related term had been used as if it were background. The corrected values used in the present manuscript are reported in the Results section.

For independent quantities, the uncertainty of background subtraction would be propagated according to $u(Cnet,j)^2 = u(CF,j)^2 + u(CBG,j)^2$. However, the individual triplicate values, the detector internal integration time, and a complete point-specific background uncertainty series were not preserved in the consolidated record. Therefore, a complete experimental standard deviation and combined measurement uncertainty cannot be reconstructed retrospectively. The available ustat values are retained only as counting-statistics indicators from the consolidated data and are not used to claim statistical significance, mechanical repeatability, or a detection threshold. In particular, small between-series differences are interpreted descriptively rather than as physically significant without a complete uncertainty budget.

To complement the absolute between-series difference criticized in the previous version, the revised analysis uses a normalized ratio and relative difference:

$$R_j = C_{net,2mm,j}\ /\ C_{net,1mm,j} \qquad (3)$$

$$\delta_j = 100 \times (R_j - 1)\ [\%] \qquad (4)$$

These normalized quantities are descriptive comparisons only because the two plates contain different local geometric conditions and were manually repositioned; they are not treated as measurements of an attenuation coefficient or as defect-classification metrics.

The sixteen net count rates were placed directly into 4 x 4 matrices following the physical grid. No numerical interpolation beyond the sixteen measured cells was used. Each map cell identifies the corresponding experimental point and net cps value, so visual features cannot be mistaken for unmeasured fine spatial structure.

2.7. Beer-Lambert reference calculation

The Beer-Lambert relation $I = I_0 \exp(-\mu x)$ was used as a theoretical narrow-beam reference rather than as an experimentally confirmed fit [3,8,9]. NIST tabulated mass attenuation coefficients for aluminum were interpolated near 0.662 MeV, giving μ/ρ approximately 7.46×10^{-2} cm^2/g. With aluminum density 2.699 g/cm^3, the corresponding linear attenuation coefficient is approximately $\mu = 0.201$ cm^{-1} [8]. The ideal primary-beam transmissions are therefore approximately 0.980 for 1 mm and 0.961 for 2 mm aluminum, corresponding to a theoretical 2 mm/1 mm transmission ratio of approximately 0.980.

An absolute thickness estimate $x = (1/\mu) \ln(I_0/I)$ requires a no-sample reference I_0 acquired with the same source, collimation, alignment, distance, detector configuration, and background treatment. No such reference was available for the final geometry. Consequently, absolute thickness values and an experimental attenuation coefficient are not reported.

2.8. Radiological protection

The experiment was conducted in a controlled laboratory environment with lead shielding, access control, reduced occupancy time, and distance from the source. These practices are consistent with the optimization principles and basic requirements applicable to industrial radiography and radiation sources [2,10]. The study did not perform a specific occupational dose assessment, and no cps-to-dose conversion was attempted. Therefore, reduced operator exposure is discussed only as a potential future benefit of remote automation, not as an experimentally demonstrated result of this dataset.

Table 1. Experimental and processing parameters of the controlled radiometric evaluation.

Parameter	Value / procedure	Interpretive status
Source	Sealed Cs-137; principal photon energy ~662 keV; source label 5.05 μCi on 15 Apr 1998	Characterization only; no cps-to-dose conversion
Collimator/shielding	Lead; nominal 120 × 120 × 120 mm; 20.0 mm central channel	Construction dimensions; no qualified shielding calculation
Detector	CZT detector; count-rate mode; software display renewed every 3 s	Model/crystal/energy calibration not preserved in record
Specimens	Aluminum; nominal 200 x 200 mm; 1 mm and 2 mm; nominal 0.5/1.0/2.0 mm holes	Hole-condition correspondence inferred, not certified point-by-point
Sampling	4 x 4 grid; P1-P16; nominal 60 mm grid spacing; serpentine sequence	Manual controlled specimen repositioning
Motion design	Cartesian X-Y architecture; nominal 1 mm command increment	Not equivalent to effective radiographic spatial resolution
Acquisition	Three source-present displayed values per point; minimum ~9 s observation	Raw triplicate values not preserved in final consolidated file
Net response	Arithmetic mean source-present cps minus point-specific recorded background	Relative radiometric quantity
Mapping	Measured 4 x 4 cells only	No interpolation beyond sampled points
Thickness reference	No no-sample I_0 acquired in final geometry	Absolute thickness not calculated

3. RESULTS AND DISCUSSION

3.1. Corrected point-by-point radiometric results

Reprocessing of the consolidated experimental record produced net count rates from 1206.00 to 2213.67 cps for the 1 mm specimen, with an overall mean of 1678.63 cps. For the 2 mm specimen, the corresponding range was 1538.00 to 2264.67 cps, with an overall mean of 1901.34 cps. The recorded point-specific background ranged from 192.67 to 376.00 cps for the 1 mm series and from 147.33 to 235.00 cps for the 2 mm series. This variation supports use of the recorded background associated with each point rather than a single global correction.

Table 2. Corrected point-by-point net count rates, available counting-statistics indicators, and normalized between-series comparison. The ± ustat values are descriptive indicators from the consolidated record, not complete measurement uncertainties.

Point	(X,Y) mm	1 mm $C_{net} \pm u_{stat}$ (cps)	2 mm $C_{net} \pm u_{stat}$ (cps)	$R = C_2/C_1$	δ (%)
P1	(10, 190)	1206.00 ± 21.71	2264.67 ± 28.46	1.878	+87.8%
P2	(70, 190)	1219.66 ± 22.65	2210.33 ± 28.55	1.812	+81.2%
P3	(130, 190)	1347.67 ± 23.15	1943.67 ± 26.63	1.442	+44.2%
P4	(190, 190)	1475.67 ± 23.68	1804.34 ± 25.64	1.223	+22.3%
P5	(190, 130)	1706.34 ± 25.20	1982.33 ± 26.77	1.162	+16.2%
P6	(130, 130)	1595.33 ± 24.42	1999.00 ± 26.86	1.253	+25.3%
P7	(70, 130)	1561.00 ± 24.28	1986.00 ± 26.72	1.272	+27.2%
P8	(10, 130)	1442.33 ± 23.48	1921.00 ± 26.36	1.332	+33.2%
P9	(10, 70)	1711.33 ± 25.19	1923.00 ± 26.36	1.124	+12.4%
P10	(70, 70)	1820.34 ± 25.99	1919.34 ± 26.36	1.054	+5.4%
P11	(130, 70)	1708.67 ± 26.36	1929.67 ± 26.35	1.129	+12.9%
P12	(190, 70)	1879.34 ± 26.51	1933.34 ± 26.40	1.029	+2.9%
P13	(190, 10)	2213.67 ± 28.41	1688.67 ± 24.84	0.763	-23.7%
P14	(130, 10)	2120.67 ± 27.92	1725.33 ± 25.10	0.814	-18.6%
P15	(70, 10)	2030.66 ± 27.27	1652.67 ± 24.52	0.814	-18.6%
P16	(10, 10)	1819.33 ± 26.01	1538.00 ± 23.70	0.845	-15.5%

The normalized ratio R varies substantially across the grid and crosses unity between the upper/middle and lower portions of the plate. Because the full uncertainty budget is unavailable, the revised manuscript does not classify any individual ratio or relative difference as statistically significant. This directly avoids interpreting small pointwise differences as definitive physical effects.

3.2. Spatial mapping and inferred geometric conditions

Figures 4 and 5 show the measured 4 x 4 matrices without numerical interpolation. The maps preserve the physical serpentine arrangement and display the point identifier and net cps inside each measured cell. Their experimentally validated contribution is therefore spatial traceability of the recorded radiometric response, not a claim of continuous high-resolution imaging.

Figure 4. Non-interpolated two-dimensional radiometric map for the nominal 1 mm aluminum specimen. Each cell represents one measured grid position and displays the point identifier and net count rate.

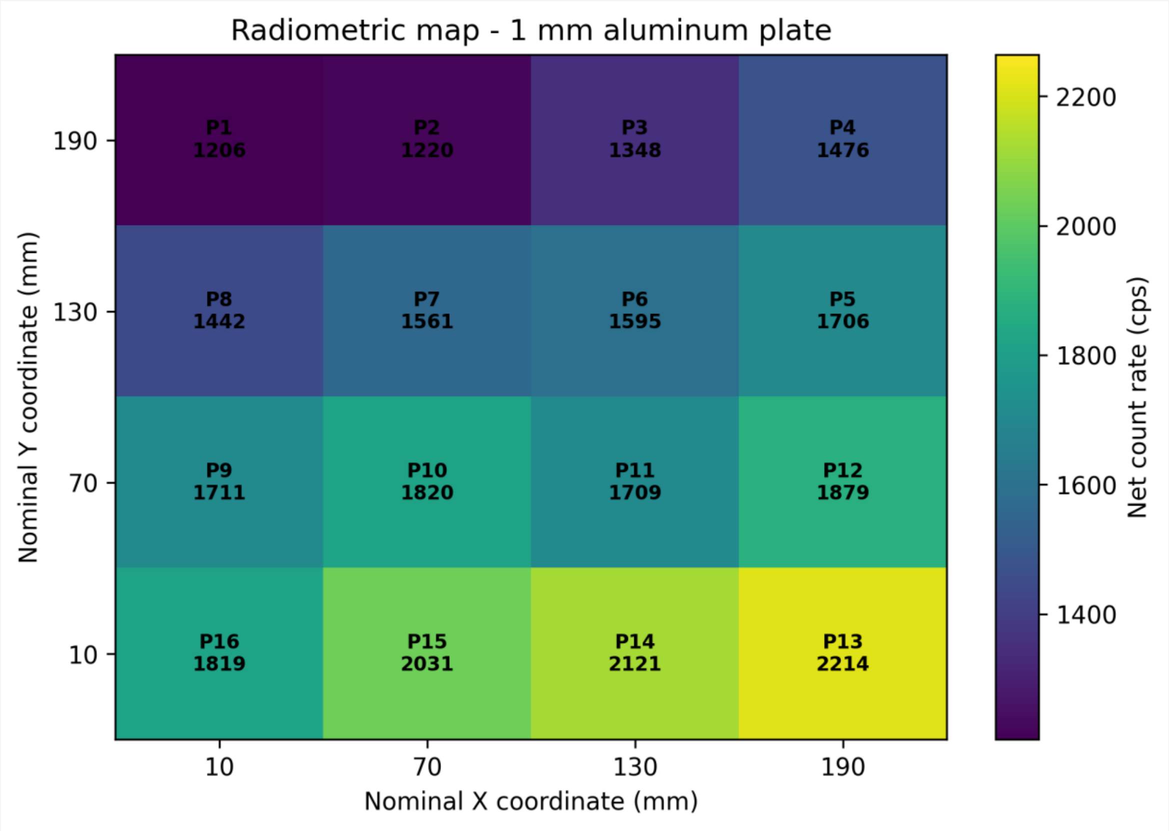

Figure 5. Non-interpolated two-dimensional radiometric map for the nominal 2 mm aluminum specimen. Each cell represents one measured grid position and displays the point identifier and net count rate.

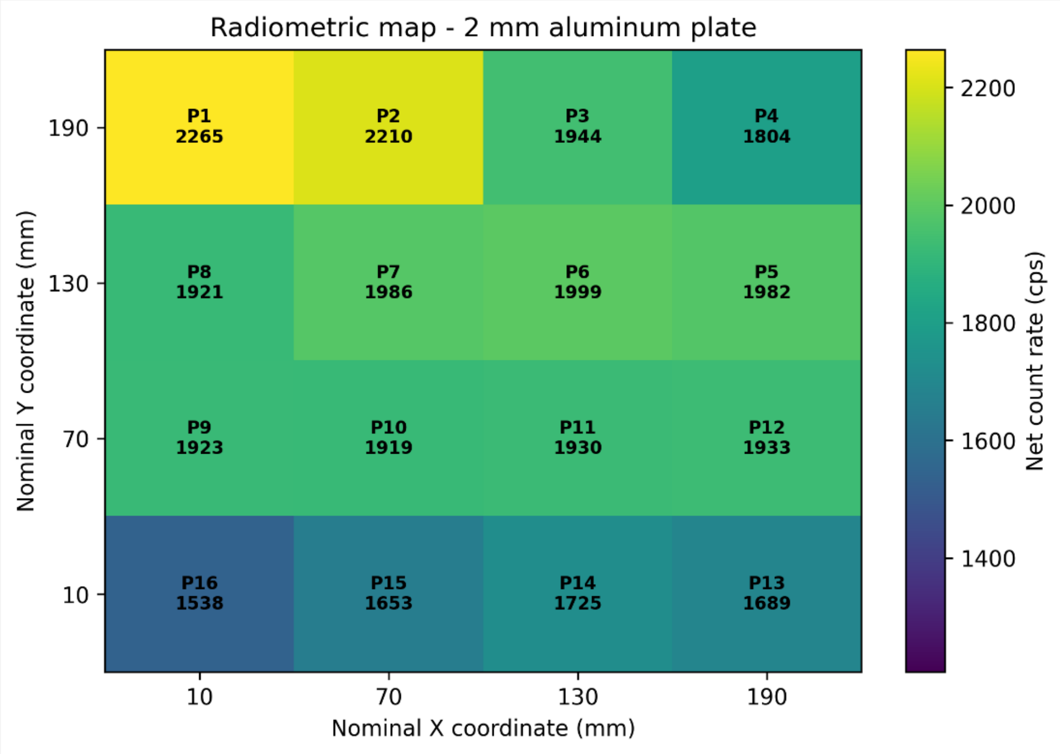

Using the inferred row-to-condition correspondence in Figure 3, the 1 mm specimen showed mean net count rates of 1312.25, 1576.25, 1779.92, and 2046.08 cps for the inferred reference, 0.5 mm, 1.0 mm, and 2.0 mm-hole groups, respectively. Relative to the inferred reference group, these correspond to descriptive contrasts of approximately +20.1%, +35.6%, and +55.9%. The 2 mm specimen showed corresponding means of 1651.17, 1926.34, 1972.08, and 2055.75 cps, or approximately +16.7%, +19.4%, and +24.5% relative to its inferred reference group.

Table 3. Mean net count rate and descriptive relative contrast by inferred geometric condition. The condition assignment is reconstructed from photographs, specimen orientation, and group behavior and is not a certified individual-defect map.

Inferred condition	1 mm points	1 mm mean cps	1 mm contrast	2 mm points	2 mm mean cps	2 mm contrast
Reference	P1-P4	1312.25	+0.0%	P13-P16	1651.17	+0.0%
0.5 mm hole	P5-P8	1576.25	+20.1%	P9-P12	1926.34	+16.7%
1.0 mm hole	P9-P12	1779.92	+35.6%	P5-P8	1972.08	+19.4%
2.0 mm hole	P13-P16	2046.08	+55.9%	P1-P4	2055.75	+24.5%

The monotonic increase of these group means within each specimen is consistent with increased transmitted response for greater inferred open area. Nevertheless, this result does not establish probability of detection, minimum detectable defect size, or certified flaw sizing because the original point-to-hole dimensional traceability and complete measurement uncertainty were not preserved. The revised interpretation is therefore limited to a spatial radiometric indication associated with inferred geometric groups.

3.3. Between-specimen comparison and Beer-Lambert reference

Figure 6. Point-by-point comparison of corrected net count rates for the 1 mm and 2 mm specimen series. The crossing response demonstrates that the two series are not monotonically ordered by nominal plate thickness.

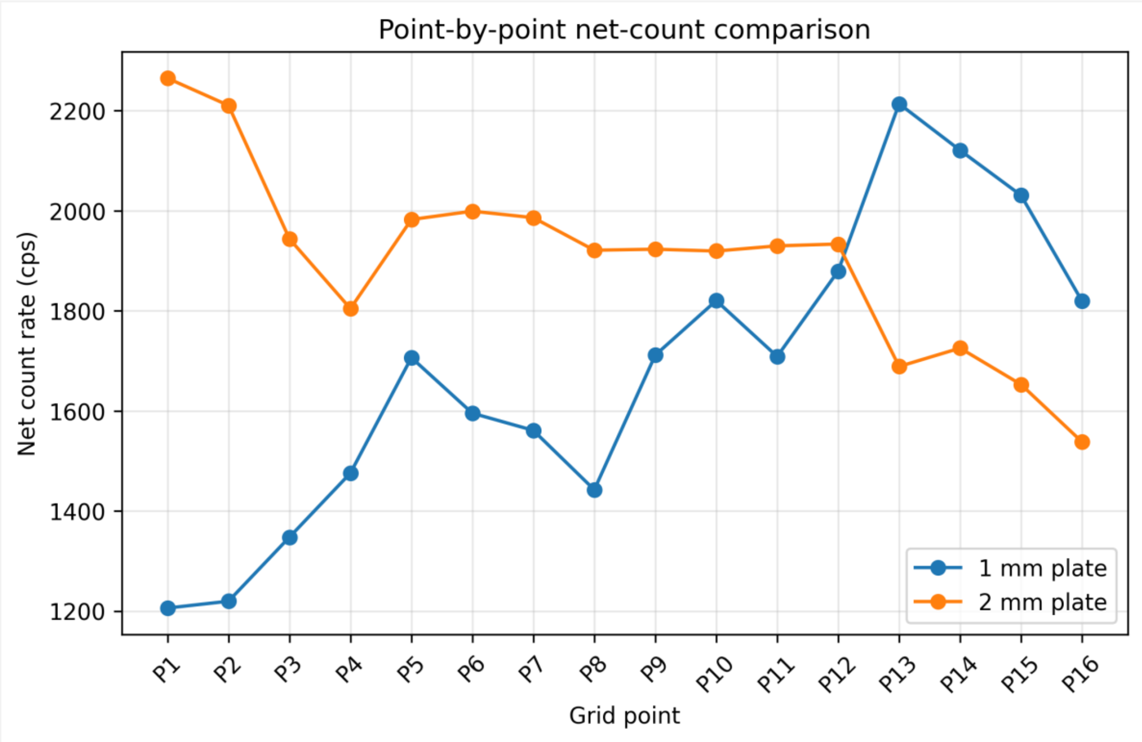

As shown in Figure 6 and Table 2, P1-P12 generally have higher net count rates in the 2 mm series, whereas P13-P16 have higher values in the 1 mm series. The overall experimental mean ratio C_2/C_1 is 1.133. This ordering is opposite to the ideal narrow-beam expectation for otherwise equivalent aluminum specimens differing only in thickness. Therefore, the two datasets cannot be used as a direct experimental determination of attenuation versus thickness.

Figure 7. Ideal Beer-Lambert primary-beam transmission for aluminum at 662 keV using μ approximately 0.201 cm⁻¹. The curve is a theoretical reference and is not a fit to the experimental data.

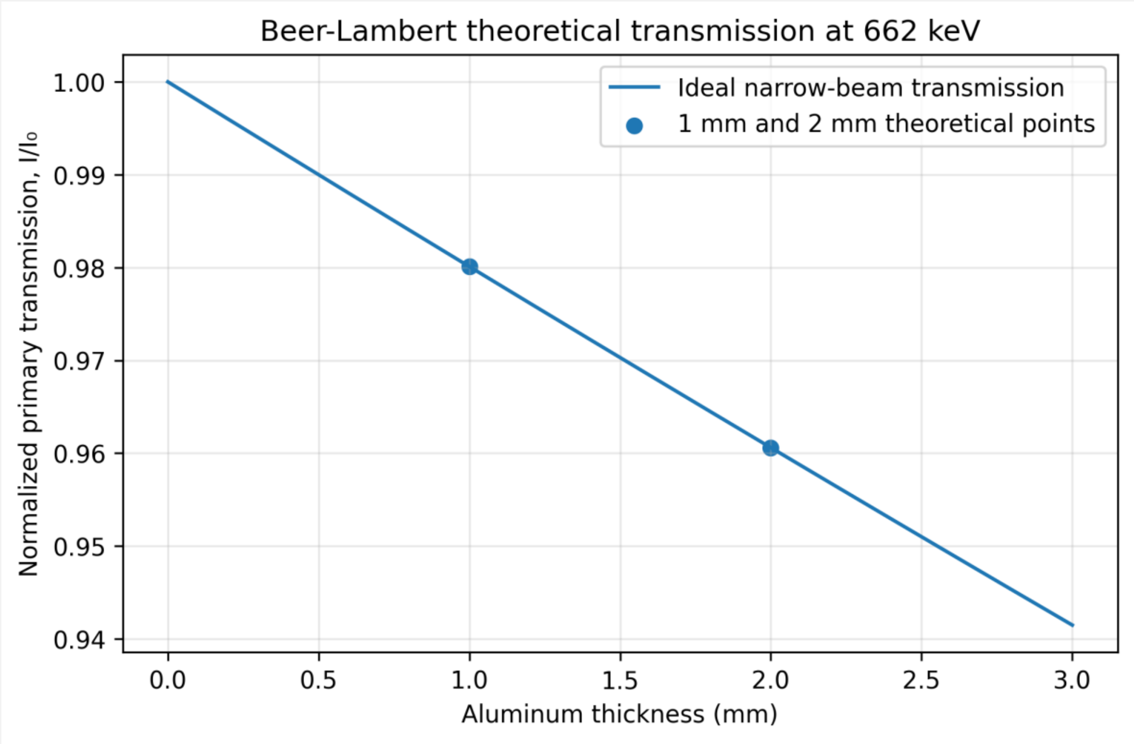

Table 4. Theoretical attenuation parameters and experimental comparison for aluminum near 662 keV.

Quantity	Value
Mass attenuation coefficient, μ/ρ	7.46×10^{-2} cm²/g
Aluminum density, ρ	2.699 g/cm³
Linear attenuation coefficient, μ	0.201 cm⁻¹
Theoretical transmission, 1 mm	0.980 (98.0%)
Theoretical transmission, 2 mm	0.961 (96.1%)
Theoretical ratio I_{2mm}/I_{1mm}	0.980
Experimental overall mean ratio	1.133
No-sample reference I_0	Not available

The discrepancy between the theoretical and measured between-specimen ordering can arise from factors that were not isolated in the original experiment, including different local perforation distributions, point-specific backgrounds, manual specimen repositioning, finite collimation, detector response, and photons scattered into the detector. At approximately 662 keV, Compton scattering is an important interaction mechanism; in a compact geometry, scattered photons may contribute to the recorded count rate [3,9]. Because this component was not independently quantified, scattering is a plausible contribution rather than a fitted correction.

The Beer-Lambert relation describes the primary-beam attenuation expected under controlled narrow-beam conditions. The theoretical difference between 1 mm and 2 mm aluminum is less than two percentage points in normalized transmission. Resolving such a small difference experimentally requires stable and equivalent geometry, an appropriate no-sample reference I_0, sufficient counting statistics, preserved replicate data, and explicit control or characterization of scattered radiation. Those conditions were not all available here; accordingly, the statement that the measurements quantitatively confirm Beer-Lambert attenuation has been removed.

3.4. Methodological limitations and requirements for automated validation

The present results validate a structured measurement pathway: acquisition of radiometric readings, point-specific background correction, association with Cartesian coordinates, organization into a 4 x 4 matrix, and generation of traceable two-dimensional maps. They do not validate the fully automated motion platform because the reported specimens were repositioned manually. Likewise, the 1 mm command increment of the engineering design is not equivalent to effective radiographic spatial resolution, which was not measured.

A quantitative defect-detection study would require specimens with certified discontinuity dimensions and coordinates, complete replicate readings, a combined uncertainty budget, repeated full scans, a defined contrast-to-noise or signal-to-noise criterion, and sufficient data to estimate a detection threshold or probability of detection. Validation of the automated platform additionally requires homing tests, measured positioning error and repeatability, cycle-time records, synchronized detector acquisition, and comparison with a controlled manual reference procedure. Occupational dose reduction would require dedicated dosimetric measurements rather than inference from automation alone.

4. CONCLUSIONS

This study presented an automated Cartesian gamma-inspection architecture and a controlled radiometric evaluation of the acquisition chain using a fixed collimated Cs-137 source, a CZT detector, and nominal 1 mm and 2 mm aluminum specimens. The experiment successfully associated corrected count-rate measurements with sixteen predefined Cartesian positions and produced non-interpolated two-dimensional radiometric maps with explicit point-to-coordinate traceability.

The corrected data show spatial variations within each specimen and an increase in grouped mean response with the inferred open-hole condition. These observations support sensitivity of the measurement chain to changes in local specimen geometry. However, the exact point-to-hole correspondence was not dimensionally certified, the complete pointwise uncertainty could not be reconstructed, and the two thickness series were not monotonic. Consequently, the results do not establish certified defect sizing, a minimum detectable defect, probability of detection, or quantitative superiority over conventional manual radiography.

The Beer-Lambert calculation predicts only a small primary-transmission difference between 1 mm and 2 mm aluminum at 662 keV. Because the experiment did not include a no-sample I_0 reference under identical geometry and did not quantify scattering, absolute thickness and an experimental attenuation coefficient were not estimated. The principal validated contribution is therefore the acquisition-background-coordinate-mapping workflow that will support subsequent integration and validation of the X-Y motion system.

Future work should preserve all individual acquisitions, use dimensionally traceable reference specimens, acquire I_0 under identical geometry, quantify combined measurement uncertainty and scattered radiation, measure mechanical positioning accuracy and repeatability, determine effective spatial resolution, establish objective contrast/SNR criteria and detection limits, and perform repeated automated scans followed by a controlled comparison with manual inspection and occupational dosimetry.

ACKNOWLEDGMENTS

The authors would like to acknowledge the support of the Instituto Militar de Engenharia (IME).

FUNDING

This research did not receive any specific grant from funding agencies in the public, commercial, or not-for-profit sectors.

CONTRIBUTORSHIP

Conceptualization: L.M.C. Silva, P.C.R. Silveira

Investigation: L.M.C. Silva

Writing - original draft: L.M.C. Silva

Writing, review and editing: L.M.C. Silva, P.C.R. Silveira

CONFLICT OF INTEREST

The authors declare that there are no conflicts of interest.

DATA AVAILABILITY STATEMENT

The authors declare that the data supporting the results of this study and the derived data supporting the conclusions of this study are available upon reasonable request to the corresponding author.

REFERENCES

[1] GUPTA, M.; KHAN, M. A.; BUTOLA, R.; SINGARI, R. M. Advances in applications of Non-Destructive Testing (NDT): A review. Advances in Materials and Processing Technologies, v. 8, n. 2, p. 2286-2307, 2022. DOI: 10.1080/2374068X.2021.1909332.

[2] INTERNATIONAL ATOMIC ENERGY AGENCY. Radiation Safety in Industrial Radiography. IAEA Safety Standards Series No. SSG-11. Vienna: IAEA, 2011.

[3] KNOLL, G. F. Radiation Detection and Measurement. 4. ed. Hoboken: John Wiley & Sons, 2010.

[4] WHITE, S. R.; MEGSON-SMITH, D. A.; ZHANG, K.; CONNOR, D. T.; MARTIN, P. G.; HUTSON, C.; HERRMANN, G.; DILWORTH, J.; SCOTT, T. B. Radiation Mapping and Laser Profiling Using a Robotic Manipulator. Frontiers in Robotics and AI, v. 7, 499056, 2020. DOI: 10.3389/frobt.2020.499056.

[5] WANG, C.; LIU, Y.; JIANG, X.; HUANG, X.; WANG, X.; XIANG, Y.; HAN, Y.; WEI, L.; ZHANG, Z. Experiment validation of the high stability of long-term transmitted gamma photon counting of a new CdZnTe semiconductor detector and its preliminary applications. Radiation Detection Technology and Methods, v. 6, p. 317-322, 2022. DOI: 10.1007/s41605-022-00330-8.

[6] MEERE, B.; DOODEMAN, S.; VIDAL, F. P.; CHANFREUT, P.; TORTA, E.; et al. X-ray Image Generation for Robotic Radiography: a Case Study on Motion Blur in Drone-Based Wind Turbine Inspections. Journal of Nondestructive Evaluation, v. 44, art. 139, 2025. DOI: 10.1007/s10921-025-01279-6.

[7] HE, Z. Review of the Shockley-Ramo theorem and its application in semiconductor gamma-ray detectors. Nuclear Instruments and Methods in Physics Research Section A, v. 463, n. 1-2, p. 250-267, 2001.

[8] NATIONAL INSTITUTE OF STANDARDS AND TECHNOLOGY. X-Ray Mass Attenuation Coefficients: Aluminum. NIST Standard Reference Database 126. Gaithersburg: NIST. Available from the NIST Physical Measurement Laboratory. Accessed: 20 Sep. 2026.

[9] ATTIX, F. H. Introduction to Radiological Physics and Radiation Dosimetry. New York: John Wiley & Sons, 1986.

[10] AUTORIDADE NACIONAL DE SEGURANÇA NUCLEAR. Norma ANSN 3.01: Requisitos Básicos de Radioproteção e Segurança Radiológica de Fontes de Radiação. Resolução CNEN 344/25, DOU 07 Jul. 2025. Brasil, 2025.

[11] SICILIANO, B.; KHATIB, O. Springer Handbook of Robotics. 2. ed. Cham: Springer, 2016.

LICENSE